CrossMark click for updates

Loss of Miro1-directed mitochondrial movement results in a novel murine model for neuron disease

Tammy T. Nguyen[a], Sang S. Oh[b], David Weaver[c], Agnieszka Lewandowska[a], Dane Maxfield[d], Max-Hinderk Schuler[a], Nathan K. Smith[a], Jane Macfarlane[a], Gerald Saunders[e], Cheryl A. Palmer[f], Valentina Debattisti[c], Takumi Koshiba[g], Stefan Pulst[h], Eva L. Feldman[b], György Hajnóczky[c], and Janet M. Shaw[a,1]

Departments of [a]Biochemistry, [f]Pathology, [h]Neurology, University of Utah School of Medicine, Salt Lake City, UT 84112; [b]Department of Neurology, University of Michigan, Ann Arbor, MI 48109; [c]MitoCare Center, Department of Pathology, Anatomy, and Cell Biology, Thomas Jefferson University, Philadelphia, PA 19107; Departments of [d]Biology and [e]Pharmacology and Toxicology, University of Utah, Salt Lake City, UT 84112; and [g]Department of Biology, Faculty of Sciences, Kyushu University, Fukuoka 812-8581, Japan

Edited* by Louis J. Ptáček, University of California, San Francisco, CA, and approved July 23, 2014 (received for review February 11, 2014)

Defective mitochondrial distribution in neurons is proposed to cause ATP depletion and calcium-buffering deficiencies that compromise cell function. However, it is unclear whether aberrant mitochondrial motility and distribution alone are sufficient to cause neurological disease. Calcium-binding mitochondrial Rho (Miro) GTPases attach mitochondria to motor proteins for anterograde and retrograde transport in neurons. Using two new KO mouse models, we demonstrate that Miro1 is essential for development of cranial motor nuclei required for respiratory control and maintenance of upper motor neurons required for ambulation. Neuron-specific loss of Miro1 causes depletion of mitochondria from corticospinal tract axons and progressive neurological deficits mirroring human upper motor neuron disease. Although *Miro1*-deficient neurons exhibit defects in retrograde axonal mitochondrial transport, mitochondrial respiratory function continues. Moreover, Miro1 is not essential for calcium-mediated inhibition of mitochondrial movement or mitochondrial calcium buffering. Our findings indicate that defects in mitochondrial motility and distribution are sufficient to cause neurological disease.

Ca^{2+}-dependent motility | Miro GTPase | mitochondrial respiration

Motor neuron diseases (MNDs), including ALS and spastic paraplegia (SP), are characterized by the progressive, length-dependent degeneration of motor neurons, leading to muscle atrophy, paralysis, and, in some cases, premature death. There are both inherited and sporadic forms of MNDs, which can affect upper motor neurons, lower motor neurons, or both. Although the molecular and cellular causes of most MNDs are unknown, many are associated with defects in axonal transport of cellular components required for neuron function and maintenance (1–6).

A subset of MNDs is associated with impaired mitochondrial respiration and mitochondrial distribution. This observation has led to the hypothesis that neurodegeneration results from defects in mitochondrial motility and distribution, which, in turn, cause subcellular ATP depletion and interfere with mitochondrial calcium ($[Ca^{2+}]_m$) buffering at sites of high synaptic activity (reviewed in ref. 7). It is not known, however, whether mitochondrial motility defects are a primary cause or a secondary consequence of MND progression. In addition, it has been difficult to isolate the primary effect of mitochondrial motility defects in MNDs because most mutations that impair mitochondrial motility in neurons also affect transport of other organelles and vesicles (1, 8–11).

In mammals, the movement of neuronal mitochondria between the cell body and the synapse is controlled by adaptors called trafficking kinesin proteins (Trak1 and Trak2) and molecular motors (kinesin heavy chain and dynein), which transport the organelle in the anterograde or retrograde direction along axonal microtubule tracks (7, 12–24). Mitochondrial Rho (Miro) GTPase proteins are critical for transport because they are the only known surface receptors that attach mitochondria to these adaptors and motors (12–15, 18, 25, 26). Miro proteins are tail-anchored in the outer mitochondrial membrane with two GTPase domains and two predicted calcium-binding embryonic fibroblast (EF) hand motifs facing the cytoplasm (12, 13, 25, 27, 28). A recent Miro structure revealed two additional EF hands that were not predicted from the primary sequence (29). Studies in cultured cells suggest that Miro proteins also function as calcium sensors (via their EF hands) to regulate kinesin-mediated mitochondrial "stopping" in axons (15, 16, 26). Miro-mediated movement appears to be inhibited when cytoplasmic calcium is elevated in active synapses, effectively recruiting mitochondria to regions where calcium buffering and energy are needed. Despite this progress, the physiological relevance of these findings has not yet been tested in a mammalian animal model. In addition, mammals ubiquitously express two Miro orthologs, Miro1 and Miro2, which are 60% identical (12, 13). However, the individual roles of Miro1 and Miro2 in neuronal development, maintenance, and survival have no been evaluated.

We describe two new mouse models that establish the importance of Miro1-mediated mitochondrial motility and distribution in mammalian neuronal function and maintenance. We show that Miro1 is essential for development/maintenance of specific cranial neurons, function of postmitotic motor neurons, and retrograde

Significance

This report probes the physiological roles of mammalian mitochondrial Rho 1 (*Miro1*), a calcium-binding, membrane-anchored GTPase necessary for mitochondrial motility on microtubules. Using two new mouse models and primary cells, the study demonstrates a specific role for *Miro1* in upper motor neuron development and retrograde transport of axonal mitochondria. Unexpectedly, *Miro1* is not essential for calcium-regulated mitochondrial movement, mitochondrial-mediated calcium buffering, or maintenance of mitochondrial respiratory activity. Nevertheless, a neuron-specific Miro1 KO mouse model displays physical hallmarks of neurological disease in the brainstem and spinal cord and develops rapidly progressing upper motor neuron disease symptoms culminating in death after approximately 4 wk. These studies demonstrate that defects in mitochondrial motility and distribution alone are sufficient to cause neurological disease.

Author contributions: T.T.N., A.L., G.H., and J.M.S. designed research; T.T.N., S.S.O., D.W., A.L., M.-H.S., N.K.S., and J.M. performed research; T.K. contributed new reagents/analytic tools; T.T.N., A.L., D.M., C.A.P., E.L.F., G.H., and J.M.S. analyzed data; T.T.N., A.L., and J.M.S. wrote the paper; G.S. provided expertise on primary cortical neuron culture; V.D. supported calcium imaging studies; S.P. provided expertise on neurological phenotype and co-mentored T.T.N.; E.L.F. provided expertise on neuropathology; and G.H. provided expertise on calcium-mediated mitochondrial motility and buffering.

The authors declare no conflict of interest.

*This Direct Submission article had a prearranged editor.

[1]To whom correspondence should be addressed. Email: shaw@biochem.utah.edu.

This article contains supporting information online at www.pnas.org/lookup/suppl/doi:10.1073/pnas.1402449111/-/DCSupplemental.

Downloaded from https://www.pnas.org by MEMORIAL SLOAN KETTERING CANCER CENTER on January 22, 2026 from IP address 140.163.254.135.

mitochondrial motility in axons. Loss of Miro1-directed retrograde mitochondrial transport is sufficient to cause MND phenotypes in mice without abrogating mitochondrial respiratory function. Furthermore, Miro1 is not essential for calcium-mediated inhibition of mitochondrial movement or $[Ca^{2+}]_m$ buffering. These findings have an impact on current models for Miro1 function and introduce a specific and rapidly progressing mouse model for MND.

Results

Loss of *Miro1* Results in Neural Respiratory Control Defects. We constructed a conditional KO allele for *Miro1* [*Miro1*^{loxP}, hereafter referred to as *Miro1* floxed (*Miro1*^{F})], in which exon 2 (encoding part of the essential GTPase I domain) is flanked with lox target sequences (loxP sites) (Fig. S1 *A–C*). Germline *Miro1* inactivation was achieved by crossing mice harboring the *Miro1*^{F} allele with a mouse line expressing Cre recombinase from the hypoxanthine-guanine phosphoribosyltransferase (*HPRT*) promoter (30) (Fig. S1 *C–E*). Mating *Miro1*$^{+/-}$ mice resulted in *Miro1*$^{-/-}$ (*Miro1* KO) animals that were cyanotic and died shortly after birth [postnatal day (P) 0] (Fig. 1*A*). *Miro1* KO mice were present in the population at the expected Mendelian frequencies (Fig. 1*B*). Fetal cardiac ultrasound at embryonic gestation day (E) 18.5 confirmed that *Miro1* KO animals were alive and had normal cardiac function before birth. The early postnatal death of *Miro1* KO animals

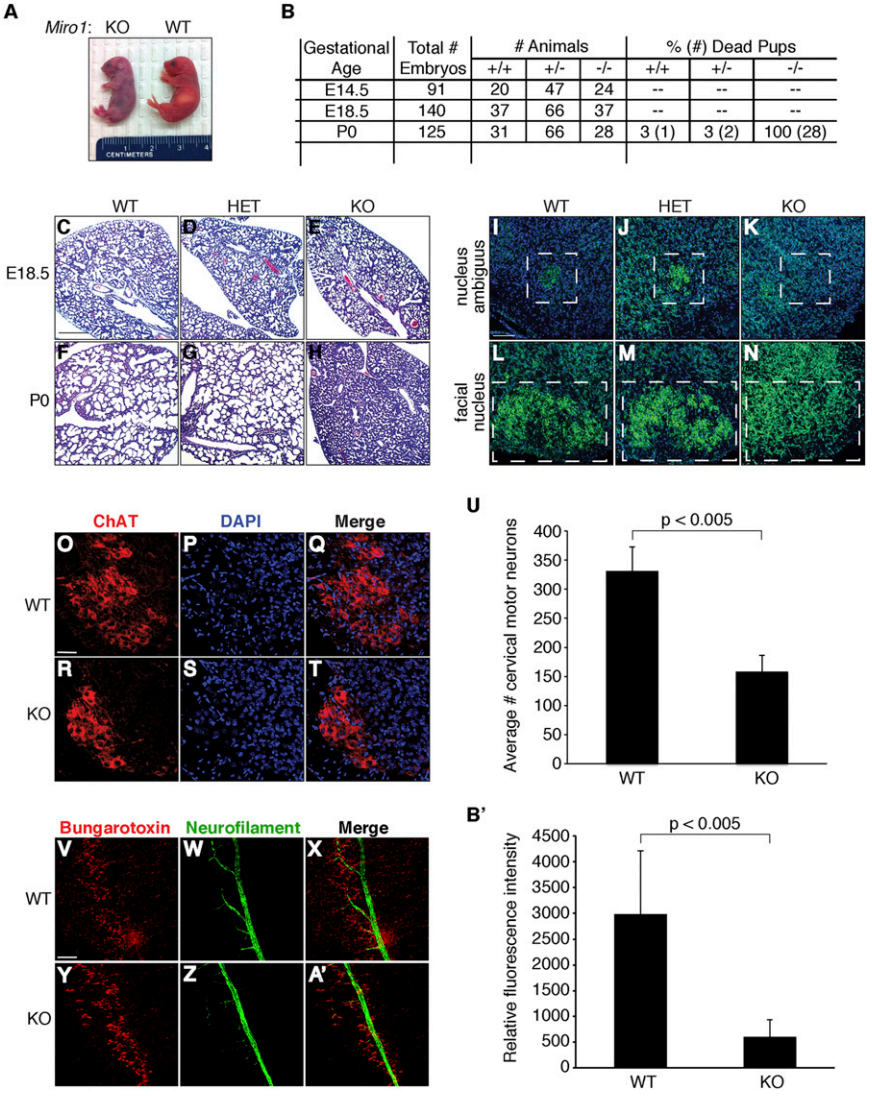

Fig. 1. *Miro1* deletion causes postnatal lethality and loss of specific neurons required for respiration. (*A*) Newborn WT and KO P0 mice after birth. Birth occurs at ~E19.5. The homozygous *Miro1* KO is cyanotic. (*B*) Loss of *Miro1* leads to postnatal lethality. (*C–H*) P0 *Miro1* KO mice fail to aerate lung tissue. H&E staining shows normal lung tissue in all genotypes before birth at E18.5 (*C–E*), aerated lung tissue in WT and HET genotypes at P0 (*F* and *G*), but unexpanded lung tissue in the KO genotype at P0 (*H*). (Scale bar: 300 μm.) (*I–N*) Loss of *Miro1* disrupts cranial nuclei formation in the hindbrain. (*I–K*) Nissl (green) and DAPI (blue) staining of the NA in the hindbrain of E18.5 animals. White dashed boxes mark the green NA region, which is present in the WT and HET genotypes but absent in the KO genotype. (*L–N*) Nissl (green) and DAPI (blue) staining of the facial nucleus (FN). White dashed boxes mark the FN region, which has defined margins in the WT and HET genotypes but not in the KO genotype. (Scale bar: 100 μm.) (*O–T*) Loss of *Miro1* reduces the number of cervical motor neurons. Representative images of anti-choline acetyltransferase (ChAT) (red, motor neurons) and DAPI (blue, nuclei) labeling of cervical motor neurons in E18.5 WT (*O–Q*) and KO (*R–T*) animals. (Scale bar: 50 μm.) (*U*) Quantification of cervical motor neurons in WT ($n = 4$) and KO ($n = 7$) animals. Data are represented as mean ± SD. (*V–Z*, and *A'*) Loss of *Miro1* reduces phrenic nerve branching. Antibungarotoxin (red, neuromuscular junctions with diaphragm) and anti-neurofilament (green, phrenic nerve) labeling of floating preparations in E18.5 WT (*V–X*) and KO (*Y–A'*) animals. (Scale bar: 100 μm.) (*B'*) Quantification of phrenic nerve branching in WT ($n = 7$) and KO ($n = 6$) animals. Data are represented as mean ± SD. (Also see Fig. S1.)

Downloaded from https://www.pnas.org by MEMORIAL SLOAN KETTERING CANCER CENTER on January 22, 2026 from IP address 140.163.254.135.

suggests that some *Miro1* functions are not shared with *Miro2*. Although the *Miro2* gene is present in *Miro1* KO mice, its expression is not up-regulated in brain tissue or *Miro1* KO mouse embryo fibroblasts (MEFs) (Fig. S1 *F–H*).

Postmortem autopsy revealed that *Miro1* KO mice had unexpanded lungs, suggesting that these animals die at birth because they fail to breathe. *Miro1* could be required for lung tissue development or for neural inputs that control respiration. However, H&E staining of *Miro1* KO lung tissue revealed no morphological abnormalities beyond a lack of lung alveoli expansion (Fig. 1 *C–H*). Thus, the postnatal respiratory failure observed in *Miro1* KO mice is not caused by gross abnormalities in lung development.

We examined the neural respiratory control pathway in *Miro1* KO mice. This pathway consists of two networks that control involuntary respiration (31). The first is the central neural respiratory network located in the brainstem, which includes cranial motor neurons of the nucleus ambiguus (NA). Although Nissl staining labeled the NA in brainstems of E15.5 and E18.5 $Miro1^{+/+}$ (WT) and $Miro1^{+/-}$ (HET) animals, this structure was absent in $Miro1^{-/-}$ (KO) mice (Fig. 1 *I–K*). We also observed marked disorganization of neurons that innervate facial muscles in *Miro1* KO mice (the facial nucleus; Fig. 1 *L–N*). By contrast, organization of cranial nerve neurons X and XII, which innervate the viscera and tongue, respectively, was normal in *Miro1* KO mice (Fig. S1*I*). Thus, loss of *Miro1* function during early development causes remarkably specific defects in brainstem cranial motor neurons.

The second network required for involuntary respiratory control is mediated by phrenic nerve innervation of the dia-

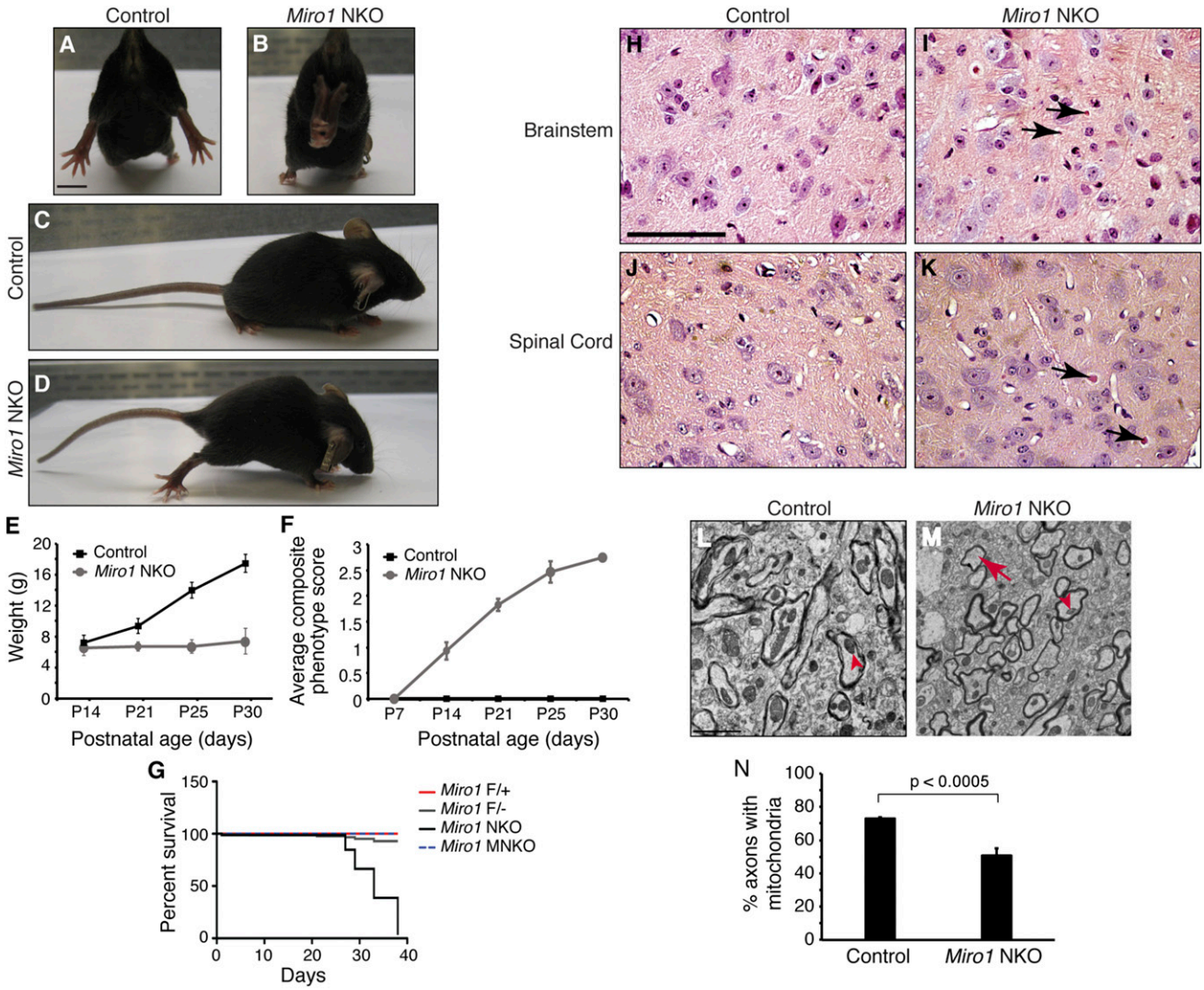

Fig. 2. *Miro1* NKO mice develop upper MND phenotypes. Images of open (*A*) and clasped (*B*) hind-limb reflex in P45 control and *Miro1* NKO ($Miro1^{F/-}$ $Eno2^{Cre/+}$) mice, respectively. (Scale bar: 10 mm.) Images of P45 control (*C*) and *Miro1* NKO (*D*) animals. NKO mice exhibit kyphosis and have stiff tails and hind limbs. (*E*) Average weights of control (black) and *Miro1* NKO (gray) mice at the indicated postnatal ages ($n = 10$). Data are represented as mean ± SD. (*F*) Average composite phenotype score for control (black) and *Miro1* NKO (gray) mice at the indicated postnatal ages ($n = 10$). Data are represented as mean ± SD. (*G*) Kaplan–Meier survival curve for control ($Miro1^{F/+}$ and $Miro1^{F/-}$; red and gray lines, respectively), *Miro1* NKO (black line), and *Miro1* MNKO ($Miro1^{F/-}$ $Mnx1^{Cre/+}$; dashed blue line) mice ($n = 10$). Representative images of H&E-stained brainstem (*H* and *I*) and anterior horn lumbar spinal cord (*J* and *K*) of P30 littermate control ($n = 6$) and *Miro1* NKO ($n = 5$) mice, respectively. Arrows mark eosinophilic Bunina-like bodies in *Miro1* NKO mice that are not present in control mice. (Scale bar: 50 μm.) Representative images (magnification: 1,000×) of lumbar spinal cord cross-sections from P30 *Miro1* control (*L*) and *Miro1* NKO (*M*) mice. Red arrowheads mark mitochondrial profiles in axons. The red arrow marks an axon lacking mitochondrial profiles in *Miro1* NKO. (Scale bar: 2 μm.) (*N*) Percentage of axons with mitochondrial profiles in control and *Miro1* NKO lumbar spinal cord sections ($n = 2{,}564$ axons from four control animals and 4,602 axons from four *Miro1* NKO animals). Data are represented as mean ± SD. (Also see Fig. S2 and Movies S1–S3.)

Downloaded from https://www.pnas.org by MEMORIAL SLOAN KETTERING CANCER CENTER on January 22, 2026 from IP address 140.163.254.135.

phragm muscle. The phrenic nerve originates from motor neurons located in the cervical spinal cord at levels C3–C5 (C, cervical spine). Anti-choline acetyltransferase (ChAT) labeling and quantification revealed that *Miro1* KO mice had significantly fewer motor neurons in this region compared with WT littermate controls (Fig. 1 *O–U*). Neurofilament labeling experiments also showed that the phrenic nerve of *Miro1* KO mice had fewer axonal branches than controls (Fig. 1 *V–B′*). These combined data indicate that death of *Miro1* KO mice is caused by specific defects in motor neurons required for breathing after birth.

***Miro1* Neuron-Specific KO Mice Develop Upper MND Phenotypes and Pathology.** The postnatal lethality of *Miro1* KO mice prevented studies of *Miro1* function in postmitotic neurons later in development. To circumvent this problem, we crossed the conditional $Miro1^{F}$ mouse with a line expressing the Cre recombinase from the enolase 2 (Eno2) promoter (32) to yield a *Miro1* neuron-specific KO (NKO; $Miro1^{F/-}$ $Eno2^{Cre/+}$) mouse. Eno2-Cre mice express the recombinase in the cerebral cortex, hippocampus, and spinal cord (Fig. S2 *A–F*). *Miro1* NKO animals were alive at birth and indistinguishable from control littermates. By P14, however, these mice displayed hind-limb clasping, an early sign of neuronal deficit (Fig. 2 *A* and *B*). As they matured, *Miro1* NKO mice failed to gain weight and developed spinal curvature (kyphosis), a stiff tail, hind-limb spasticity, and severe movement defects (Fig. 2 *C–F* and Movies S1–S3). These phenotypes resemble symptoms observed in human upper MND, became more severe with age, and resulted in premature death by approximately P35 (Fig. 2*G*).

Further analyses identified a histological marker of neurological disease in *Miro1* NKO mice. The cerebral cortex and hippocampal regions of NKO mice were similar to those of littermate controls (Fig. S2 *G–J*). However, the brainstem and lumbar spinal cord regions of the *Miro1* NKO mice contained aggregate bodies that were absent in control animals (Fig. 2 *H–K*). These structures resemble Bunina bodies, which are eosinophilic inclusions commonly observed in degenerating neurons of patients with ALS (33–35). By contrast, the Bunina-like structures in *Miro1* KO tissues appeared to be extracellular and may correspond to remnants of dead neurons. The combination of motor defects and histological markers for MND indicates that loss of *Miro1* causes MND in mice.

Given the known role of *Miro1* in mitochondrial movement, we postulated that defects in *Miro1* NKO mice might be accompanied by changes in axonal mitochondrial distribution. We tested this hypothesis by quantifying negative-stained mitochondrial profiles in lumbar spinal cord axons of *Miro1* NKO mice at P25–P30, ages when movement phenotypes are severe. Only 49.5% of lumbar spinal cord axons in *Miro1* NKO mice contained mitochondrial profiles, compared with 69.6% in littermate controls (Fig. 2 *L–N*). There were no obvious changes in axon myelination of *Miro1* NKO mice relative to controls. Thus, the movement phenotypes observed in *Miro1* NKO mice are most likely due to defects in mitochondrial distribution that lead to motor neuron dysfunction.

***Miro1* Is Required for Retrograde Axonal Mitochondrial Movement.** The behaviors and histological markers observed in *Miro1* NKO mice are consistent with a role for *Miro1* in maintenance of upper motor neurons. In support of this interpretation, Mnx1-Cre driven KO of $Miro1^{F}$ in motor neurons of the developing CNS (excluding the brain) caused no obvious phenotypes [Fig. 2*G*; *Miro1* MNKO ($Miro1^{F/-}$ $Mnx1^{Cre/+}$) mouse] (36, 37). Thus, defects observed in *Miro1* NKO mice are likely caused by loss of *Miro1* function in upper motor neurons that originate in the cerebral cortex and travel down the spinal cord. To explore the cellular basis of this defect, we examined the distribution of mitochondria and their molecular motors in primary cortical cultures from $Miro1^{+/+}$, $Miro1^{+/-}$, and $Miro1^{-/-}$ animals. In colocalization studies, anti-Tom20–labeled mitochondria were present in MAP-2–labeled dendritic processes of *Miro1* WT, HET, and KO primary cortical neurons (Fig. S3 *A–I*). Moreover, colocalization of axonal mitochondria with a kinesin (Fig. S3 *J–L*) or dynein (Fig. S3 *M–O*) motor was similar in cultures from all three genotypes.

To determine whether *Miro1* loss altered axonal mitochondrial movement, we performed confocal time-lapse imaging on primary *Miro1* WT and KO cortical neurons transfected with GFP-outer membrane protein 25 (OMP25) (mito-GFP) (Fig. 3 *A* and *B*). Kymographs generated from time-lapse images revealed the behavior of individual mitochondria within an axon (50–150 μm in length) (38). Stationary mitochondria appear as vertical lines, and moving mitochondria appear as diagonal lines, with the slope representing the velocity (Fig. 3 *C* and *D*). Approximately 35% of mitochondria were motile in *Miro1* KO cortical neurons, similar to the percentage observed in *Miro1* WT (Fig. 3*E*) and reported in the literature for WT neurons (20, 39, 40). However, the motile mitochondria in *Miro1* KO axons spent less time in motion compared with WT (Fig. 3*F*). These data raised the possibility that processivity of mitochondrial movement is impaired in *Miro1* KO cortical neurons. Indeed, we observed that mitochondria in *Miro1* KO axons exhibited a fourfold reduction in overall retrograde velocity compared with WT (Fig. 3*G*). By contrast, no significant difference in *Miro1* KO anterograde velocity was observed relative to WT (Fig. 3*G*). Additional analysis revealed that the instantaneous velocities of axonal mitochondria in primary cortical neurons were similar to those reported previously and no different between *Miro1* KO and WT (41) (Fig. S3*P*). Finally, we observed a twofold reduction in retrograde run length in the *Miro1* KO cortical neurons, although anterograde run lengths were unaffected (Fig. 3*H*). These data indicate that loss of *Miro1* in cortical neurons preferentially affects retrograde axonal mitochondrial movement.

***Miro1* Loss Causes Mitochondrial Distribution Defects Without Concomitant Changes in Respiration.** It is hypothesized that damaged axonal and/or synaptic mitochondria need to be shuttled back to the cell body for general repair or turnover by mitophagy. In addition, a previous study reported that pharmacological disruption of mitochondrial respiration increased retrograde mitochondrial transport in axons (42). According to this model, a defect in Miro1-mediated retrograde movement is predicted to interfere with mitochondrial quality control and cause the accumulation of respiratory compromised mitochondria. However, histochemical enzyme assays of cytochrome *c* oxidase (COX) and succinate dehydrogenase (SDH) revealed no COX-negative, SDH-positive neurons in the cerebral cortex or hippocampus of *Miro1* WT and KO embryos (Fig. 4 *A–D* and Fig. S4). In addition, negative staining and transmission EM detected mitochondria with normal cristae ultrastructure in axons of *Miro1* WT and NKO animals, suggesting that mitochondrial respiration was intact (Fig. 4 *E* and *F*). Thus, mitochondrial respiration likely continues in these affected tissues when *Miro1* is disrupted. We also examined mitochondrial membrane potential in WT and KO primary cortical neurons by double labeling with potential-independent (MitoTracker Green; Molecular Probes) and potential-dependent [tetramethylrhodamine methyl ester (TMRM); Biotium] dyes. There were no differences in the pattern of mitochondrial staining (Fig. 4 *G–J*), and for both genotypes, the majority of mitochondria were labeled with TMRM. Variability in the intensity of TMRM staining within and between different WT and KO axons was observed; however, both cultures displayed the same range of TMRM/MitoTracker Green fluorescence intensity ratios (Fig. S4*E*). The fact that TMRM labeled mitochondria of KO axons indicates that these organelles continue to respire.

Because it is not possible to measure mitochondrial respiratory capacity directly using mixed primary neuronal cultures, we generated MEFs from *Miro1* WT, HET, and KO mice. In

Downloaded from https://www.pnas.org by MEMORIAL SLOAN KETTERING CANCER CENTER on January 22, 2026 from IP address 140.163.254.135.

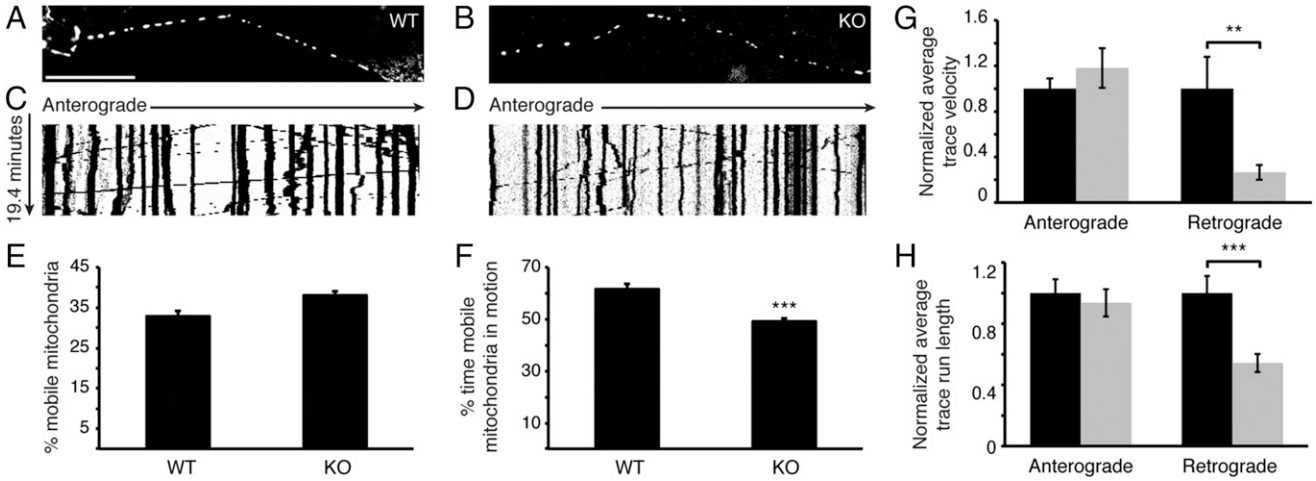

Fig. 3. *Miro1* is required for efficient retrograde axonal mitochondrial movement. (*A* and *B*) Representative images of GFP-labeled mitochondria in axons of primary cortical neurons. (Scale bar: 50 μm.) Representative kymographs of mitochondrial movement in axons of *Miro1* WT (*C*) and KO (*D*) primary cortical neurons. The anterograde direction is indicated. (*E*) Average percentage of mobile mitochondria in *Miro1* WT ($n = 36$) and KO ($n = 65$) axons ($P = 0.162$). (*F*) Average percentage of time moving mitochondria remain in motion in *Miro1* WT ($n = 229$) and KO ($n = 427$) axons (***$P < 0.0001$). (*G*) Normalized average anterograde and retrograde trace velocities of *Miro1* WT (black, $n = 119$ anterograde and $n = 110$ retrograde) and KO (gray, $n = 220$ anterograde and $n = 207$ retrograde) mitochondria (**$P < 0.005$). (*H*) Normalized average anterograde and retrograde trace run lengths of *Miro1* WT (black, $n = 119$ anterograde and $n = 110$ retrograde) and KO (gray, $n = 220$ anterograde and $n = 207$ retrograde) mitochondria (***$P < 0.0001$). In *E–H*, error bars are mean ± SEM. (Also see Fig. S3.)

Miro1 WT and HET MEFs, mitochondria labeled with MitoTracker had the characteristic tubular morphology and were distributed throughout the cytoplasm and in filopodia (Fig. 5 *A*, *B*, and *D* and Fig. S5 *A–C*). By contrast, mitochondria in the *Miro1* KO MEFs were clustered around the nucleus (perinuclear) and absent from filopodia (Fig. 5 *C* and *D* and Fig. S5 *D–F*). Fluorescence recovery after photobleaching and time-lapse imaging indicated that some mitochondria in KO MEFs were motile over short distances despite the distribution defect (Fig. S5 *G–P*). Further analyses revealed no gross changes in the organization of actin, intermediate filaments, or microtubules (Fig. S5 *Q–Y*). The morphology and distribution of the endoplasmic reticulum (ER), peroxisomes, and lysosomes were also unaffected in these cells (Fig. S5 *Z–H′*). The mitochondrial distribution defect in *Miro1* KO MEFs was rescued by overexpression of *Miro1* (three spliced variants) or *Miro2* (Fig. 5*E*). The ability of both *Miro1* and *Miro2* to rescue mitochondrial distribution defects in *Miro1* KO MEFs indicates that the two genes have some overlapping functions. In the case of *Miro2*, this rescue requires overexpression, because *Miro2* transcript and protein are present but not up-regulated in *Miro1* KO MEFs, which display a mitochondrial distribution defect (Fig. S1 *F–H*).

Despite the mitochondrial distribution defect in *Miro1* KO MEFs, we observed no change in inner mitochondrial membrane potential. There were no differences in the pattern of mitochondrial staining when *Miro1* WT, Het, and KO MEFs were dual-labeled with potential-independent (mito-GFP) and potential-dependent (MitoTracker Red; Invitrogen) markers (Fig. 5 *G–R*). Moreover, direct measurements of oxygen consumption rates (an indicator of mitochondrial respiratory capacity) revealed no differences between *Miro1* WT, HET, and KO MEFs (Fig. 5*F*). Thus, although *Miro1* is required for proper mitochondrial distribution in MEFs, this defect does not detectably alter mitochondrial membrane potential or respiratory function. Our combined cellular analyses suggest that MND-like phenotypes in *Miro1* NKO mice are a direct result of defects in mitochondrial motility and distribution.

***Miro1* Is Not Essential for $[Ca^{2+}]_m$ Uptake or Calcium Inhibition of Mitochondrial Motility.** A previous overexpression study suggested that the Ca^{2+}-binding activity of Miro1 EF-hand motifs is not required for mitochondrial-mediated calcium buffering (26). However, it is not known whether changes in mitochondrial distribution caused by *Miro1* loss affect the efficiency of calcium uptake by the organelle. To test the physiological importance of *Miro1* for $[Ca^{2+}]_m$ uptake, cytosolic calcium ($[Ca^{2+}]_c$) and $[Ca^{2+}]_m$ concentrations were measured simultaneously in intact *Miro1* WT and KO MEFs transfected with mitochondrial-targeted inverse pericam (a $[Ca^{2+}]_m$ sensor) and loaded with fura2/acetoxymethyl ester (a ratiometric cytoplasmic calcium indicator dye) (26). Temporal changes in $[Ca^{2+}]_m$ and $[Ca^{2+}]_c$ concentrations were measured as fluctuations in fluorescence intensity of fura2 and inverse pericam in response to increasing intracellular calcium. To stimulate a global increase in $[Ca^{2+}]_c$, the ER calcium store was first depleted by treatment with thapsigargin (an inhibitor of the ER Ca^{2+} ATPase) in Ca^{2+}-free buffer, whereupon readdition of $CaCl_2$ evokes entry of exogenously added calcium via plasma membrane store-operated channels. Using this approach, we observed no difference in the rate or extent of $[Ca^{2+}]_m$ rise in *Miro1* WT and KO MEFs (Fig. 6 *A* and *B*). Thus, *Miro1* does not directly affect mitochondrial Ca^{2+} uptake. More importantly, the defective distribution and perinuclear clustering of mitochondria in *Miro1* KO MEFs does not appear to interfere with mitochondrial buffering of $[Ca^{2+}]_c$.

We also tested the effect of *Miro1* loss on calcium-mediated inhibition of mitochondrial movement. In this case, *Miro1* WT and KO MEFs expressing mitochondrial matrix-targeted YFP were loaded with fura2 to monitor $[Ca^{2+}]_c$ concentration. Exogenously added Ca^{2+} was used to set $[Ca^{2+}]_c$ at concentrations known to allow basal motility ($[Ca^{2+}]_c < 100$ nM) or to cause partial ($[Ca^{2+}]_c = 400–600$ nM) or maximal ($[Ca^{2+}]_c > 1$ μM) motility inhibition, as determined by calculating the differences between successive images in a time series (43) (Fig. S6 *A* and *B*). To ensure rapid equilibration of the cytoplasm with added extracellular calcium $[Ca^{2+}]$, cells were initially depleted of the cation by incubation with EGTA, thapsigargin, and ionomycin (a Ca^{2+} ionophore). As shown in Fig. 6*C*, dose–response plots of normalized motility inhibition as a function of calcium concen-

Downloaded from https://www.pnas.org by MEMORIAL SLOAN KETTERING CANCER CENTER on January 22, 2026 from IP address 140.163.254.135.

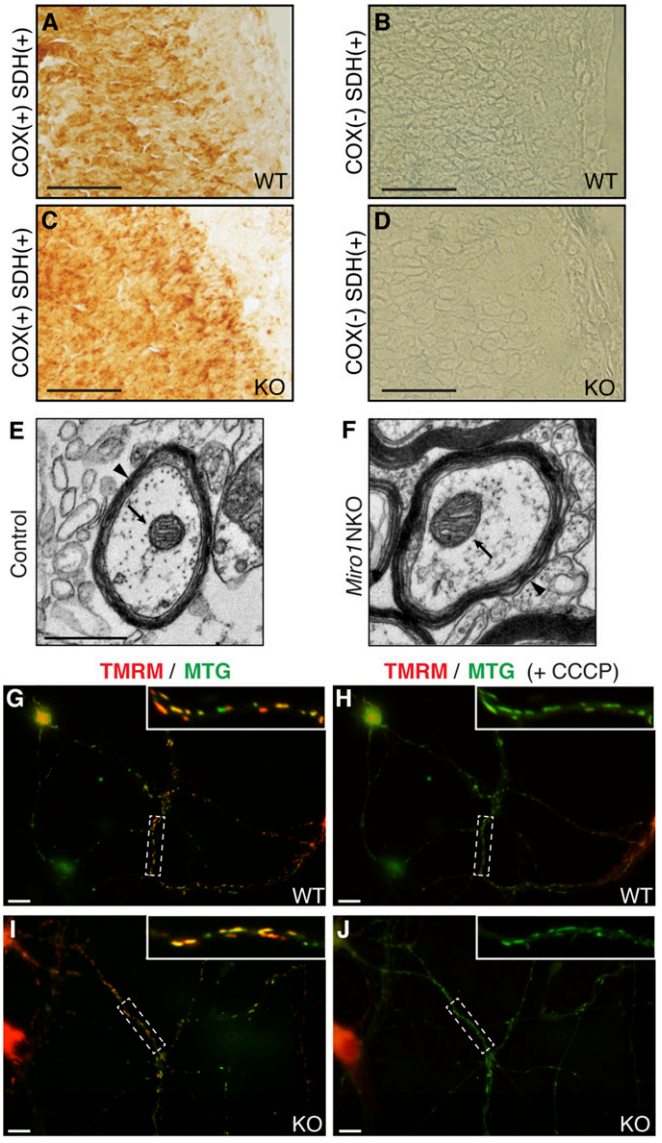

Fig. 4. *Miro1* loss does not abolish mitochondrial bioenergetic function. COX/SDH activity histochemical double labeling of representative cryosections of cerebral cortex of E18.5 *Miro1* WT (*A* and *B*, $n = 3$) and KO (*C* and *D*, $n = 3$) embryos. Brown staining reflects COX activity (*A* and *C*), and SDH activity results in blue staining (*B* and *D*) (controls treated with COX inhibitor). (Scale bars: 50 μm.) (Also see Fig. S4.) (*E* and *F*) Representative cross-sectional images of axons from the lumbar spinal cord of P30 *Miro1* WT and NKO animals. Arrows mark cristae structure within mitochondrial profiles. Arrowheads mark myelin sheaths. (Scale bar: 0.5 μm.) Double labeling of primary cortical *Miro1* WT (*G* and *H*) and KO (*I* and *J*) neurons with mitochondrial membrane potential-independent MitoTracker Green (MTG) and potential-dependent TMRM (red). Panels show the same field of view before (*G* and *I*) and 2 min after (*H* and *J*) treatment with 10 μM carbonyl cyanide m-chlorophenyl hydrazone (CCCP) ("+CCCP"). (*G–J*, *Insets, Upper Right*) Magnified views of the boxed area are displayed as *Insets* in *G–J*. (Scale bar: 10 μm. Magnification: 3×.)

tration were essentially indistinguishable for *Miro1* WT and KO MEFs. *Miro1* WT and KO MEFs also displayed similar IC_{50} measurements of 400–500 nM $[Ca^{2+}]_c$. Moreover, the extent of maximum inhibition was unaffected by loss of *Miro1*. The average ratio of pixel counts at maximum inhibition as a fraction of basal motility calculated for each cell was identical (12% for both WT and KO) (Fig. S6 *A* and *B*).

Importantly, Miro1 was also not essential for Ca^{2+}-dependent mitochondrial motility inhibition in cortical neurons. Addition of 1.2 mM calcium to calcium-depleted cells (leading to a rise in $[Ca^{2+}]_c$ from ∼100 nM to 300–1,000 nM) resulted in a significant decrease in mitochondrial motility in both WT and KO axons (paired *t* test of nonnormalized motility figures before and after calcium, $P < 0.001$ for both) (Fig. 6 *D* and *E*). The degree of motility inhibition was not significantly different between WT and KO axons. Further addition of calcium (5 mM) and ionomycin (10 μM) resulted in total arrest of motility in both genotypes (Fig. 6*E* and Fig. S6*C*), although calcium may not be the only mechanism at play under the latter conditions. Threshold values for motility calculation were determined algorithmically and were not significantly different between WT and KO in any of the experiments. Together, these results demonstrate that the loss of *Miro1* does not prevent the Ca^{2+}-dependent inhibition of mitochondrial motility and argue against an essential role for *Miro1* in calcium control of mitochondrial motility.

Discussion

Previous work established that Miro GTPases function with adaptors and motor proteins to transport mitochondria along cytoskeletal tracks (7, 22, 44). Additional investigations in cultured cells suggested that Miro function would be critical in neurons, which move mitochondria long distances to sites where ATP and calcium buffering are needed. The studies described here reveal an unexpectedly specific requirement for *Miro1* in upper motor neuron development and postmitotic function. Moreover, targeted disruption of *Miro1* in the cerebral cortex causes retrograde mitochondrial motility defects in cortical neurons, depletion of mitochondria from corticospinal tract axons, and rapidly progressing upper MND without concomitant changes in mitochondrial respiration.

The germ-line *Miro1* KO mouse completes embryogenesis but fails to breathe and dies at birth. Our analyses indicate that loss of the brainstem NA contributes to this breathing defect. It is possible that Miro1 is required for the survival of motor neurons that form the NA. Preliminary studies of E15.5 *Miro1* KO embryos showed reduced labeling with apoptotic markers in this region compared with WT. Thus, the neuronal cell bodies that normally populate the NA may simply be absent, rather than dying. Studies are underway to determine whether *Miro1* is required for specification, migration, or postmigration survival of precursors that populate this structure. We also documented a decrease in the number of phrenic nerve branches that innervate the diaphragm in KO animals. It has been known for many years that mitochondria are enriched in active growth cones and at sites of neuronal branching (45). In *Miro1*-deficient animals, mitochondrial depletion from these sites could interfere with branch initiation or compromise maintenance of branches after they form. In support of this model, depletion of the Miro adaptor Trak1 is reported to decrease axonal branching (24). In addition, a specific kinase pathway was recently shown to support axon branching in cortical neurons by promoting immobilization of mitochondria at presynaptic sites via the docking protein syntaphilin (39, 46–48). Although the neuronal defects described here are the most likely cause of early mortality in *Miro1* KO mice, changes in additional neuronal populations or tissues may also contribute to this phenotype.

Before this study, the available evidence suggested that Miro1 and Miro2 interchangeably form complexes with adaptors (Trak1 and Trak2 in mammals or Milton in *Drosophila*) and motors (kinesin heavy chain and dynein) to transport mitochondria in both the anterograde and retrograde directions (12–22, 24, 25). Our finding that *Miro1* loss selectively affects retrograde mitochondrial transport and run length in cortical axons demonstrates that Miro1 and Miro2 contribute unequally to bidirectional mitochondrial movement in neurons. Additional evidence supports the idea that the composition of mitochondrial movement complexes modulates their activities. In hippocampal

Downloaded from https://www.pnas.org by MEMORIAL SLOAN KETTERING CANCER CENTER on January 22, 2026 from IP address 140.163.254.135.

Downloaded from https://www.pnas.org by MEMORIAL SLOAN KETTERING CANCER CENTER on January 22, 2026 from IP address 140.163.254.135.

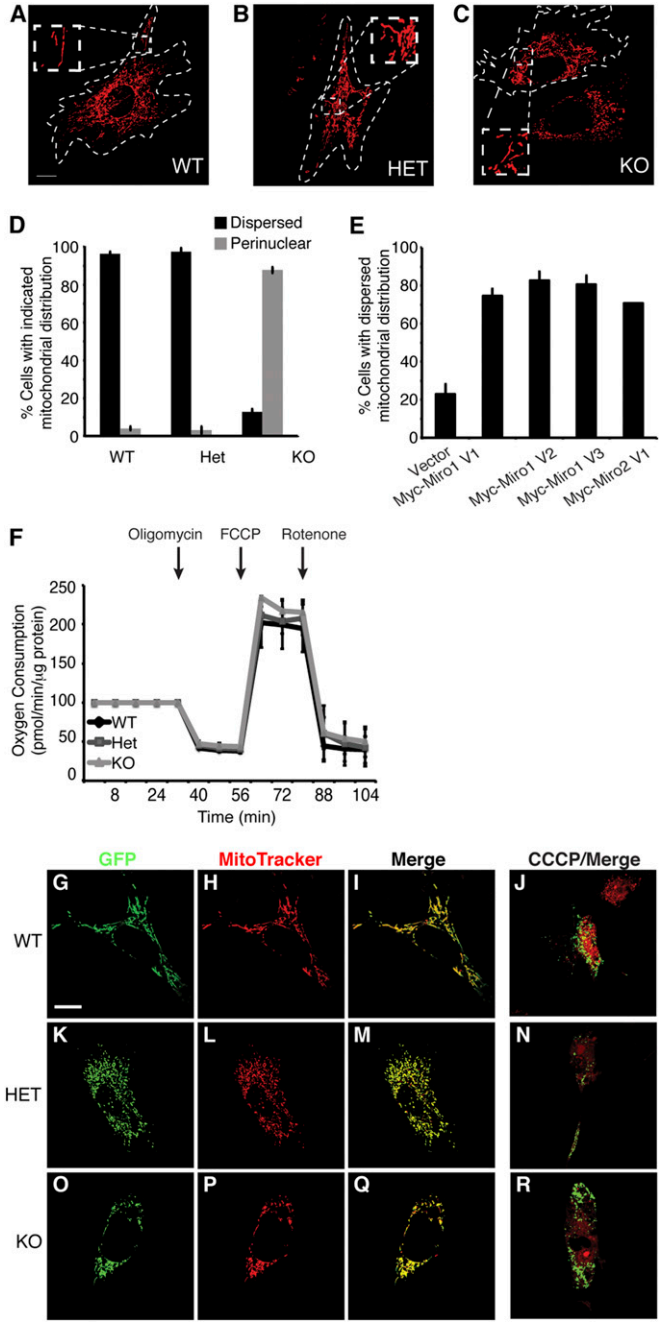

Fig. 5. *Miro1* loss does not affect mitochondrial bioenergetic function in MEFs. (*A–C*) Mitochondrial morphology and distribution in the indicated MEF genotypes were examined after staining with MitoTracker CM-H_2XROS (red). Boxed areas are magnified to show mitochondrial morphology. (Scale bar: 10 μm.) (*D*) Quantification of dispersed (black bars) vs. perinuclear (gray bars) mitochondrial distribution in primary MEFs (n = 100). Error bars represent mean ± SD from three independent experiments. (*E*) Quantification of mitochondrial distribution in *Miro1* KO MEFs overexpressing Myc-tagged Miro1 splice variants and Miro2 (n = 100). Error bars represent mean ± SD from three independent experiments. (*F*) Primary oxygen consumption capacity was examined in the *Miro1* WT, HET, and KO MEFs after stressing mitochondrial respiration with the indicated drugs. Data are represented as mean ± SD. FCCP, carbonilcyanide p-triflouromethoxyphenylhydrazone. (*G–R*) Mitochondrial membrane potential (ΔΨ) determined by comparing mitochondrial GFP-OMP25 (*G*, *K*, and *O;* potential-independent, green) and MitoTracker Red CM-H_2XROS (*H*, *L*, and *P*; potential-dependent, red) labeling in merged images (*I*, *M*, and *Q*) using MEFs of the indicated genotypes. (Scale bar: 10 μm.) (*J*, *N*, and *R*) Merged images show lack of colocalization when mitochondrial respiratory activity (and MitoTracker Red CM-H_2XROS accumulation) is dissipated by CCCP treatment. (Scale bar: 20 μm.) (Also see Fig. S5.)

neurons, the Trak1 and Trak2 adaptors differentially control mitochondrial movement in axons and dendrites, and they preferentially bind either the kinesin or dynein motor proteins, respectively (24). Although not yet tested, Miro1 and Miro2 may also bind adaptors (and, indirectly, motors) with different affinities and preferentially transport mitochondria in the retrograde or anterograde direction. The effect of Miro1 disruption on retrograde movement could also be indirect. Anterograde and retrograde motors have been shown to bind mitochondria simultaneously or associate with mitochondria moving in both directions (16, 49, 50). Thus, the selective activation and inactivation of bound motors could coordinate bidirectional movement of the organelle (51). Loss of Miro1 from the mitochondrial surface might disrupt interactions between, or regulation of, Miro2-associated kinesin and dynein motors in a manner that preferentially impairs retrograde transport.

The retrograde transfer defect in cultured neurons does not result in the same type of axonal mitochondrial depletion we observed in lumbar spinal cord sections from *Miro1* NKO mice (Fig. 2 *L–N*). Axons analyzed in culture are much shorter than those of the corticospinal tract in the mouse, which could explain this difference. In addition, the process of culturing cortical tissue may alter both the type and physiology of neurons relative to those in vivo. Finally, cells in culture, which are chronologically "younger" than neurons of a P30 *Miro1* NKO mouse, may not be mature enough to display this phenotype.

The retrograde transport defect we observe in cortical neurons may not be recapitulated in nonpolarized cells. When Miro1 is absent from both MEFs (Fig. 4 *E* and *F*) and astrocytes (Fig. S3*H*), mitochondria collapse near the nuclear periphery. In MEFs, dynein moves mitochondria toward microtubule minus ends near the nucleus and kinesin moves mitochondria toward microtubule plus ends at the cell periphery. Thus, the perinuclear mitochondrial clustering in MEFs is predicted to result from defects in kinesin-mediated motility toward the cell periphery. Alternatively, loss of Miro1 in these cells may cause mitochondria to become anchored near the nucleus. In particular, physical connections between the ER membrane and the outer mitochondrial membrane are known to coordinate the functions of these organelles in many organisms (52). Fluorescently tagged Miro proteins localize at these ER-mitochondrial attachment sites in both yeast and mammalian cells (53). Interestingly, a role for the yeast Miro homolog in separating newly divided mitochondria from ER-mitochondrial attachment sites was recently reported (54). Whether this function is conserved in mammals and is responsible for the mitochondrial perinuclear clustering that occurs when Miro1 is absent is under investigation.

It is well established that elevated cytoplasmic calcium inhibits mitochondrial movement in a variety of cell types, allowing the organelle to collect at sites where energy is needed (7, 17). In addition, mitochondria accumulate and sequester the elevated cytoplasmic calcium associated with synaptic activity in neurons (55). Failure to buffer elevated calcium is implicated in neuronal cell death via excitotoxicity (2, 56). Previous work strongly suggested that Miro proteins were the $[Ca^{2+}]_m$ sensors, because Ca^{2+} binding to the EF-hand motifs in Miro appeared to halt kinesin-driven mitochondrial movement (15, 16, 26). Thus, we were surprised to find that calcium-mediated mitochondrial stopping and $[Ca^{2+}]_m$ buffering were unchanged when Miro1 was absent. It is possible that *Miro2* is responsible for the bulk of the calcium sensing that occurs in vivo. There may also be a Miro-independent calcium-sensing mechanism responsible for regulating

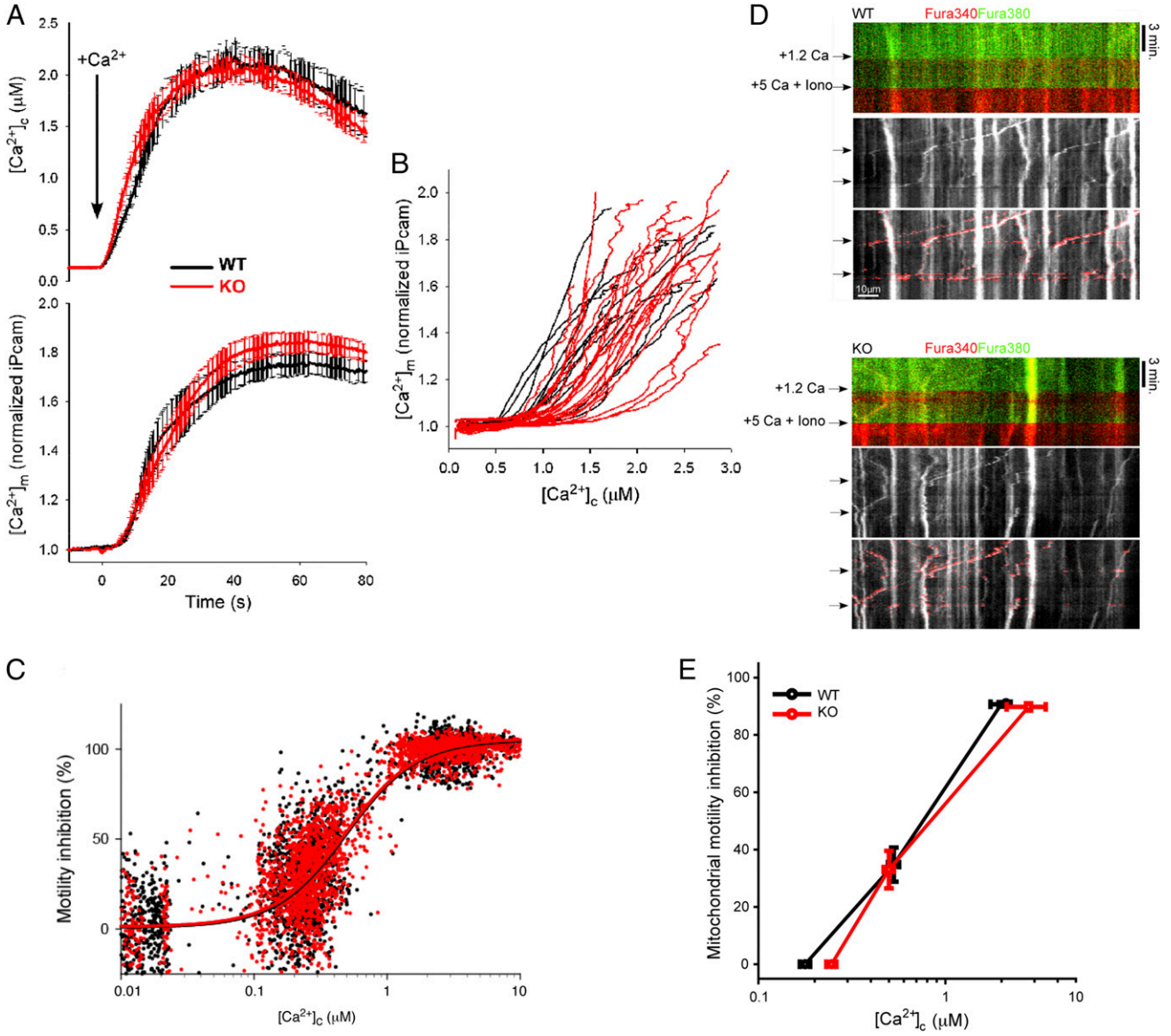

Fig. 6. *Miro1* loss does not interfere with mitochondrial Ca^{2+} uptake or Ca^{2+}-mediated inhibition of mitochondrial motility. (*A*) Graphs depict the average synchronized traces ± SEM of $[Ca^{2+}]_c$ (*Upper*) and $[Ca^{2+}]_m$ (*Lower*) in the indicated MEFs during store-operated calcium entry as determined by fura2 and inverse pericam (iPcam), respectively. Included in the means are all cells that showed maximum $[Ca^{2+}]_c$ in the range of 1–3 μm (WT, $n = 11$; KO, $n = 23$). (*B*) $[Ca^{2+}]_m$ as a function of $[Ca^{2+}]_c$ during the rising phase of $[Ca^{2+}]_c$ is shown for each cell included in the means. (*C*) Dose–response relationship between $[Ca^{2+}]_c$ and motility inhibition in *Miro1* WT (black; IC_{50}: 498 ± 18 nM, $n = 20$) and KO (red; IC_{50}: 492 ± 15 nM, $n = 22$). (*D*) Kymographs generated from single processes in WT or KO primary cortical neurons. Overlay of fura2 fluorescence at 340 nm (red) and 380 nm (green) excitation (*Top*), MitoTracker Green fluorescence (*Middle*, grayscale), and MitoTracker Green overlaid with calculated motility (*Bottom*, red). (Scale bar: 10 μm.) Iono, ionomycin. (*E*) Plot shows the mean ± SEM of $[Ca^{2+}]_c$ and mitochondrial motility inhibition in cortical neurons at rest, after 1.2 mM $CaCl_2$, and after 5 mM $CaCl_2$ plus Iono. Data are derived from those processes where $[Ca^{2+}]_c$ rose to the range of 0.3–1.0 μm after the addition of 1.2 mM $CaCl_2$. (WT, $n = 33$ from three embryos; KO, $n = 23$ from five embryos). (Also see Fig. S6.)

mitochondrial movement under normal conditions or when Miro1 is absent.

The *Miro1* NKO mice develop age-dependent, progressive neurological symptoms that most closely resemble SP (57, 58). Although mitochondrial distribution defects accompanied by mitochondrial respiratory defects are associated with a subset of MNDs, only a few of these are attributable to primary mutations that disrupt mitochondrial respiration (6, 59). In the remaining cases, it has been difficult to unravel the relative contributions of mitochondrial distribution defects or mitochondrial respiratory defects to disease progression. We now show that loss of mammalian Miro1 function can have a negative impact on mitochondrial distribution without disrupting mitochondrial respiratory function. When combined with the severe neurological phenotypes observed in the *Miro1* NKO mouse, these findings demonstrate that primary defects in mitochondrial motility and distribution can cause neurological disease.

Materials and Methods

Mouse Experiments. Generation of $Miro1^{F}$, $Miro1^{-/-}$ KO, and NKO mice is described in *SI Materials and Methods*. All experiments were approved by the University of Utah Institutional Animal Care and Use Committee. All controls were phenotypic WT littermates of the mutant animals ($Miro1^{F/+}$ $Eno2^{Cre/+}$, $Miro1^{F/+}$ $Eno2^{+/+}$, and $Miro1^{F/-}$ $Eno2^{+/+}$). A blinded examiner performed behavioral analysis and physical examinations. Mice were

Downloaded from https://www.pnas.org by MEMORIAL SLOAN KETTERING CANCER CENTER on January 22, 2026 from IP address 140.163.254.135.

weighed and rated for kyphosis, hind-limb clasping, and a ledge-walking test, and were observed during ambulation at P21, P25, and P30. P7 and P14 mice were weighed and rated for kyphosis and hind-limb clasping. Using these metrics, a phenotype severity score was assigned using a predetermined rating scale, with 0 being WT and 3 being most severe (60).

For fetal ultrasound, pregnant mice (E18.5) anesthetized with isoflurane were maintained on a heated stage, with continuous monitoring of the ECG and respiration. Embryos were monitored within 45 min of laparotomy. The order of embryos was noted for genotype correlation. A Vevo 660 ultrasound machine (VisualSonics) with a 40-MHz transducer was used for imaging. Heart rates were determined by M-mode ultrasound.

MEFs and Cortical Neuronal Culture. MEFs were isolated from *Miro1* KO, Het, and WT littermate E14.5 embryos and immortalized by lentiviral transduction with large T antigen (61). Primary MEF cells were cultured in DMEM (Invitrogen) supplemented with 10% (vol/vol) FBS (Sigma), L-glutamine (Invitrogen), penicillin/streptomycin (Invitrogen), and 50 mM β-mercaptoethanol (Sigma). Lipofectamine 2000 (Invitrogen) was used to transfect either 5 μg of plasmids harboring Myc-tagged variants of Miro1 and Miro2 or 1 μg of a plasmid harboring GFP-OMP25 (provided by the laboratory of D. Chan, California Institute of Technology, Pasadena, CA) (62).

Primary mixed cultures of cortical neurons were prepared from four WT and five KO E14.5 mice, as described previously (63, 64). The cultures were plated at a low density (130,000–150,000 cells) on poly-L-lysine–coated, eight-well, glass-bottomed chamber slides (Lab-Tek II; Thermo Scientific), or 12-mm glass coverslips placed in 60-mm dishes. Cultures were maintained in a humidified incubator at 37 °C with 5% (vol/vol) CO_2 for 1–2 wk. The culture medium was replaced with fresh plating media [MEM (Sigma), 10% (vol/vol) horse serum (Invitrogen), 5,000 units of penicillin and 5,000 μg of streptomycin, 30 mM glucose, 4 mM L-glutamine, and 8 μg of Ara-C (Sigma)] every 2–3 d. Before imaging and transient transfection, cortical culture media were changed to Neurobasal A feeding media [Neurobasal A supplemented with B27 (Invitrogen), 500 units of penicillin and 500 μg of streptomycin, 0.5 mM GlutaMax (Invitrogen), and 12 mM glucose]. At 7–9 d in vitro, each well/coverslip of cortical cultures was transfected with 1 μg of GFP-OMP25 using 2.5 μL of Lipofectamine 2000, and was imaged 1–4 d later.

Additional details are provided in *SI Materials and Methods*.

ACKNOWLEDGMENTS. We thank personnel at the University of Utah Core Facilities for assistance, especially S. Tamowski (Transgenic/Gene Targeting Mouse Facility), L. Nikolova, and N. Chandler (Electron Microscopy Core). We thank the Pathology Cores for Animal Research of the Unit for Laboratory Animal Medicine at the University of Michigan. We are grateful to L. McGill (veterinary pathologist at ARUP Laboratories) for expert advice. We also thank J. Rutter, K. Thomas, A. Boulet, L. Hoffman, A. Shakya, S. Hansen, R. Dorsky, K. Wilcox, M. Williams, and V. Maricq (University of Utah) and J. Hayes (University of Michigan) for assistance and discussions. P. Aspenström, D. Chan, and D. Ward provided Miro2 antibody and the GFP-OMP25 and LAMP1-mCherry expression constructs, respectively. This work was funded by National Institutes of Health Grants GM84970 and GM53466 (to J.M.S.), F31 NS080342 (to T.T.N.), R01 NS033123 (to S.P.), DK051526 (to G.H.), and R24 082841 (to E.L.F.); the American Diabetes Association, Program for Neurology Research and Discovery (E.L.F.); the A. Alfred Taubman Medical Research Institute (E.L.F.); and Japan Society for the Promotion of Science Grant KAKENHI 25115515 (to T.K.). C.A.P. was partially supported by a National Multiple Sclerosis Society grant awarded to J. Kriesel.

1. Perlson E, Maday S, Fu MM, Moughamian AJ, Holzbaur ELF (2010) Retrograde axonal transport: Pathways to cell death? *Trends Neurosci* 33(7):335–344.
2. Sheng Z-H, Cai Q (2012) Mitochondrial transport in neurons: Impact on synaptic homeostasis and neurodegeneration. *Nat Rev Neurosci* 13(2):77–93.
3. Shirendeb UP, et al. (2012) Mutant huntingtin's interaction with mitochondrial protein Drp1 impairs mitochondrial biogenesis and causes defective axonal transport and synaptic degeneration in Huntington's disease. *Hum Mol Genet* 21(2):406–420.
4. Sterky FH, Lee S, Wibom R, Olson L, Larsson N-G (2011) Impaired mitochondrial transport and Parkin-independent degeneration of respiratory chain-deficient dopamine neurons in vivo. *Proc Natl Acad Sci USA* 108(31):12937–12942.
5. Wang X, Perry G, Smith MA, Zhu X (2010) Amyloid-beta-derived diffusible ligands cause impaired axonal transport of mitochondria in neurons. *Neurodegener Dis* 7(1-3):56–59.
6. Ferreirinha F, et al. (2004) Axonal degeneration in paraplegin-deficient mice is associated with abnormal mitochondria and impairment of axonal transport. *J Clin Invest* 113(2):231–242.
7. Schwarz TL (2013) Mitochondrial trafficking in neurons. *Cold Spring Harb Perspect Biol* 5(6).
8. Chevalier-Larsen ES, Wallace KE, Pennise CR, Holzbaur ELF (2008) Lysosomal proliferation and distal degeneration in motor neurons expressing the G59S mutation in the p150Glued subunit of dynactin. *Hum Mol Genet* 17(13):1946–1955.
9. Dixit R, Ross JL, Goldman YE, Holzbaur ELF (2008) Differential regulation of dynein and kinesin motor proteins by tau. *Science* 319(5866):1086–1089.
10. Kasher PR, et al. (2009) Direct evidence for axonal transport defects in a novel mouse model of mutant spastin-induced hereditary spastic paraplegia (HSP) and human HSP patients. *J Neurochem* 110(1):34–44.
11. Xia C-H, et al. (2003) Abnormal neurofilament transport caused by targeted disruption of neuronal kinesin heavy chain KIF5A. *J Cell Biol* 161(1):55–66.
12. Fransson A, Ruusala A, Aspenström P (2003) Atypical Rho GTPases have roles in mitochondrial homeostasis and apoptosis. *J Biol Chem* 278(8):6495–6502.
13. Fransson S, Ruusala A, Aspenström P (2006) The atypical Rho GTPases Miro-1 and Miro-2 have essential roles in mitochondrial trafficking. *Biochem Biophys Res Commun* 344(2):500–510.
14. Glater EE, Megeath LJ, Stowers RS, Schwarz TL (2006) Axonal transport of mitochondria requires milton to recruit kinesin heavy chain and is light chain independent. *J Cell Biol* 173(4):545–557.
15. Macaskill AF, et al. (2009) Miro1 is a calcium sensor for glutamate receptor-dependent localization of mitochondria at synapses. *Neuron* 61(4):541–555.
16. Wang X, Schwarz TL (2009) The mechanism of Ca2+ -dependent regulation of kinesin-mediated mitochondrial motility. *Cell* 136(1):163–174.
17. Liu X, Hajnóczky G (2009) Ca2+-dependent regulation of mitochondrial dynamics by the Miro-Milton complex. *Int J Biochem Cell Biol* 41(10):1972–1976.
18. MacAskill AF, Brickley K, Stephenson FA, Kittler JT (2009) GTPase dependent recruitment of Grif-1 by Miro1 regulates mitochondrial trafficking in hippocampal neurons. *Mol Cell Neurosci* 40(3):301–312.
19. Russo GJ, et al. (2009) Drosophila Miro is required for both anterograde and retrograde axonal mitochondrial transport. *J Neurosci* 29(17):5443–5455.
20. Brickley K, Smith MJ, Beck M, Stephenson FA (2005) GRIF-1 and OIP106, members of a novel gene family of coiled-coil domain proteins: Association in vivo and in vitro with kinesin. *J Biol Chem* 280(15):14723–14732.
21. Stowers RS, Megeath LJ, Górska-Andrzejak J, Meinertzhagen IA, Schwarz TL (2002) Axonal transport of mitochondria to synapses depends on milton, a novel Drosophila protein. *Neuron* 36(6):1063–1077.
22. Saxton WM, Hollenbeck PJ (2012) The axonal transport of mitochondria. *J Cell Sci* 125(Pt 9):2095–2104.
23. Stephenson FA (2013) Revisiting the TRAK Family of Proteins as Mediators of GABAA Receptor Trafficking. *Neurochem Res* 39(6):1–5.
24. van Spronsen M, et al. (2013) TRAK/Milton motor-adaptor proteins steer mitochondrial trafficking to axons and dendrites. *Neuron* 77(3):485–502.
25. Guo X, et al. (2005) The GTPase dMiro is required for axonal transport of mitochondria to Drosophila synapses. *Neuron* 47(3):379–393.
26. Saotome M, et al. (2008) Bidirectional Ca2+-dependent control of mitochondrial dynamics by the Miro GTPase. *Proc Natl Acad Sci USA* 105(52):20728–20733.
27. Frederick RL, McCaffery JM, Cunningham KW, Okamoto K, Shaw JM (2004) Yeast Miro GTPase, Gem1p, regulates mitochondrial morphology via a novel pathway. *J Cell Biol* 167(1):87–98.
28. Koshiba T, et al. (2011) Structure-function analysis of the yeast mitochondrial Rho GTPase, Gem1p: Implications for mitochondrial inheritance. *J Biol Chem* 286(1):354–362.
29. Klosowiak JL, et al. (2013) Structural coupling of the EF hand and C-terminal GTPase domains in the mitochondrial protein Miro. *EMBO Rep* 14(11):968–974.
30. Tang SH, Silva FJ, Tsark WM, Mann JR (2002) A Cre/loxP-deleter transgenic line in mouse strain 129S1/SvImJ. *Genesis* 32(3):199–202.
31. Caubit X, et al. (2010) Teashirt 3 regulates development of neurons involved in both respiratory rhythm and airflow control. *J Neurosci* 30(28):9465–9476.
32. Kwon C-H, et al. (2006) Neuron-specific enolase-cre mouse line with cre activity in specific neuronal populations. *Genesis* 44(3):130–135.
33. Kato T, Katagiri T, Hirano A, Sasaki H, Arai S (1988) Sporadic lower motor neuron disease with Lewy body-like inclusions: A new subgroup? *Acta Neuropathol* 76(2):208–211.
34. Hart MN, Cancilla PA, Frommes S, Hirano A (1977) Anterior horn cell degeneration and Bunina-type inclusions associated with dementia. *Acta Neuropathol* 38(3):225–228.
35. Takahashi H, Ohama E, Ikuta F (1991) Are bunina bodies of endoplasmic reticulum origin? An ultrastructural study of subthalamic eosinophilic inclusions in a case of atypical motor neuron disease. *Acta Pathol Jpn* 41(12):889–894.
36. Arber S, et al. (1999) Requirement for the homeobox gene Hb9 in the consolidation of motor neuron identity. *Neuron* 23(4):659–674.
37. Yang X, et al. (2001) Patterning of muscle acetylcholine receptor gene expression in the absence of motor innervation. *Neuron* 30(2):399–410.
38. Mukherjee A, et al. (2011) Automated kymograph analysis for profiling axonal transport of secretory granules. *Med Image Anal* 15(3):354–367.
39. Courchet J, et al. (2013) Terminal axon branching is regulated by the LKB1-NUAK1 kinase pathway via presynaptic mitochondrial capture. *Cell* 153(7):1510–1525.
40. Wang X, et al. (2011) PINK1 and Parkin target Miro for phosphorylation and degradation to arrest mitochondrial motility. *Cell* 147(4):893–906.
41. Li Y, et al. (2009) HUMMR, a hypoxia- and HIF-1alpha-inducible protein, alters mitochondrial distribution and transport. *J Cell Biol* 185(6):1065–1081.
42. Miller KE, Sheetz MP (2004) Axonal mitochondrial transport and potential are correlated. *J Cell Sci* 117(Pt 13):2791–2804.

Downloaded from https://www.pnas.org by MEMORIAL SLOAN KETTERING CANCER CENTER on January 22, 2026 from IP address 140.163.254.135.

43. Yi M, Weaver D, Hajnóczky G (2004) Control of mitochondrial motility and distribution by the calcium signal: A homeostatic circuit. *J Cell Biol* 167(4):661–672.
44. Frederick RL, Shaw JM (2007) Moving mitochondria: Establishing distribution of an essential organelle. *Traffic* 8(12):1668–1675.
45. Morris RL, Hollenbeck PJ (1993) The regulation of bidirectional mitochondrial transport is coordinated with axonal outgrowth. *J Cell Sci* 104(Pt 3):917–927.
46. Chen Y, Sheng ZH (2013) Kinesin-1-syntaphilin coupling mediates activity-dependent regulation of axonal mitochondrial transport. *J Cell Biol* 202(2):351–364.
47. Kang JS, et al. (2008) Docking of axonal mitochondria by syntaphilin controls their mobility and affects short-term facilitation. *Cell* 132(1):137–148.
48. Lao G, et al. (2000) Syntaphilin: A syntaxin-1 clamp that controls SNARE assembly. *Neuron* 25(1):191–201.
49. Hirokawa N, Sato-Yoshitake R, Yoshida T, Kawashima T (1990) Brain dynein (MAP1C) localizes on both anterogradely and retrogradely transported membranous organelles in vivo. *J Cell Biol* 111(3):1027–1037.
50. Pilling AD, Horiuchi D, Lively CM, Saxton WM (2006) Kinesin-1 and Dynein are the primary motors for fast transport of mitochondria in Drosophila motor axons. *Mol Biol Cell* 17(4):2057–2068.
51. Ligon LA, Tokito M, Finklestein JM, Grossman FE, Holzbaur EL (2004) A direct interaction between cytoplasmic dynein and kinesin I may coordinate motor activity. *J Biol Chem* 279(18):19201–19208.
52. Rowland AA, Voeltz GK (2012) Endoplasmic reticulum-mitochondria contacts: Function of the junction. *Nat Rev Mol Cell Biol* 13(10):607–625.
53. Kornmann B, Osman C, Walter P (2011) The conserved GTPase Gem1 regulates endoplasmic reticulum-mitochondria connections. *Proc Natl Acad Sci USA* 108(34): 14151–14156.
54. Murley A, et al. (2013) ER-associated mitochondrial division links the distribution of mitochondria and mitochondrial DNA in yeast. *Elife (Cambridge)* 2(e00422):e00422.
55. Nicholls DG (2009) Mitochondrial calcium function and dysfunction in the central nervous system. *Biochim Biophys Acta* 1787(11):1416–1424.
56. Nicotera P, Bano D (2003) The enemy at the gates. Ca2+ entry through TRPM7 channels and anoxic neuronal death. *Cell* 115(7):768–770.
57. Blackstone C (2012) Cellular pathways of hereditary spastic paraplegia. *Annu Rev Neurosci* 35:25–47.
58. Fink JK (2013) Hereditary spastic paraplegia: clinico-pathologic features and emerging molecular mechanisms. *Acta Neuropathol* 126(3):307–328.
59. Bross P, et al. (2008) The Hsp60-(p.V98I) mutation associated with hereditary spastic paraplegia SPG13 compromises chaperonin function both in vitro and in vivo. *J Biol Chem* 283(23):15694–15700.
60. Guyenet SJ, et al. (2010) A simple composite phenotype scoring system for evaluating mouse models of cerebellar ataxia. *J Vis Exp* 39:1787–1789.
61. Zhu JY, Abate M, Rice PW, Cole CN (1991) The ability of simian virus 40 large T antigen to immortalize primary mouse embryo fibroblasts cosegregates with its ability to bind to p53. *J Virol* 65(12):6872–6880.
62. Chen H, Chomyn A, Chan DC (2005) Disruption of fusion results in mitochondrial heterogeneity and dysfunction. *J Biol Chem* 280(28):26185–26192.
63. Alex AB, Baucum AJ, Wilcox KS (2006) Effect of Conantokin G on NMDA receptor-mediated spontaneous EPSCs in cultured cortical neurons. *J Neurophysiol* 96(3): 1084–1092.
64. Otto JF, Kimball MM, Wilcox KS (2002) Effects of the anticonvulsant retigabine on cultured cortical neurons: Changes in electroresponsive properties and synaptic transmission. *Mol Pharmacol* 61(4):921–927.

Downloaded from https://www.pnas.org by MEMORIAL SLOAN KETTERING CANCER CENTER on January 22, 2026 from IP address 140.163.254.135.